Princeton Plasma Physics Laboratory

PPPL- 4752

PPPL- 4752

Delta f Monte Carlo Calculation Of Neoclassical Transport In Perturbed Tokamaks

Kimin Kim, Jong-Kyu Park, Gerrit Kramer and Allen H. Boozer

April, 2012

PPPL PRINCETON PLASMA PHYSICS LABORATORY

Prepared for the U.S. Department of Energy under Contract DE-AC02-09CH11466.

Princeton Plasma Physics Laboratory
Report Disclaimers

Full Legal Disclaimer

Trademark Disclaimer

PPPL Report Availability

Princeton Plasma Physics Laboratory:

http://www.pppl.gov/techreports.cfm

Office of Scientific and Technical Information (OSTI):

http://www.osti.gov/bridge

Related Links:

U.S. Department of Energy

Office of Scientific and Technical Information

Fusion Links

δf Monte Carlo calculation of neoclassical transport in perturbed tokamaks

Kimin Kim,[1] Jong-Kyu Park,[1] Gerrit J. Kramer,[1] and Allen H. Boozer[2]

[1] *Princeton Plasma Physics Laboratory, Princeton, NJ 08543*

[2] *Columbia University, New York, NY 10027*

(Dated: April 9, 2012)

Non-axisymmetric magnetic perturbations can fundamentally change neoclassical transport in tokamaks by distorting particle orbits on deformed or broken flux surfaces. This so-called non-ambipolar transport is highly complex, and eventually a numerical simulation is required to achieve its precise description and understanding. A new δf particle code (POCA) has been developed for this purpose using a modified pitch angle collision operator preserving momentum conservation. POCA was successfully benchmarked for neoclassical transport and momentum conservation in axisymmetric configuration. Non-ambipolar particle flux is calculated in the non-axisymmetric case, and results show a clear resonant nature of non-ambipolar transport and magnetic braking. Neoclassical toroidal viscosity (NTV) torque is calculated using anisotropic pressures and magnetic field spectrum, and compared with the generalized NTV theory. Calculations indicate a clear δB^2 dependence of NTV, and good agreements with theory on NTV torque profiles and amplitudes depending on collisionality.

I. INTRODUCTION

Non-axisymmetric magnetic perturbations can fundamentally change the neoclassical transport in tokamaks by distorting particle orbits on deformed or broken flux surfaces. Understanding transport under non-axisymmetric magnetic perturbations is a critical issue for ITER and future fusion devices where non-axisymmetric perturbations are potentially important control elements to actively stabilize locked modes, edge localized modes, and resistive wall modes [1]. Neoclassical transport with non-axisymmetry, often called Neoclassical Toroidal Viscosity (NTV) transport in tokamaks, is intrinsically non-ambipolar [2], and highly complex depending on parametric regimes. Progress has been substantially made by various analytical attempts [3–5], but the analytic studies were limited in narrow regimes or strong approximations on particle orbits, geometries, and collisions. Therefore a numerical approach with more realistic physics models is eventually required to achieve a precise and self-consistent description. This paper reports the development of new δf particle code and successful calculations of non-ambipolar transport and NTV torque in perturbed tokamaks.

A new δf particle code, POCA (Particle Orbit Code for Anisotropic pressures) has been developed for transport study in perturbed tokamaks. POCA aims to calculate fundamental properties of neoclassical transport with non-axisymmetric magnetic perturbations and to efficiently provide viable information to a 3D equilibrium solver. POCA follows guiding center orbit motions in 3D spatial and pitch angle spaces on the flux coordinates and solves Fokker-Planck equation with δf Monte Carlo method to obtain the perturbed distribution function δf. Collisions are calculated using a modified pitch angle scattering collision operator, in which a momentum restoring term is included in a simple manner to conserve toroidal momentum. POCA follows a conventional way in calculating the neoclassical transport properties but is developed to easily handle the information of non-axisymmetric magnetic perturbations.

POCA is a local code which calculates the particle transport at a single flux surface, so it is more efficient than global code. In addition, δf Monte Carlo method applied to POCA is much more efficient than standard Monte Carlo method by a factor of 10^4, which means δf code requires less particles by 10^{-4} than standard Monte Carlo code to achieve the same accuracy. Such efficient and convenient features of POCA enable a coupling with 3D perturbed equilibrium code [6], where an anisotropic pressure tensor is required to compute non-ideal force balance.

This paper describes a development of POCA and neoclassical transport calculations with non-axisymmetric magnetic perturbations. After successful benchmarking in axisymmetry, POCA calculates non-ambipolar transport and NTV torque in non-axisymmetry, which shows a clear resonant nature of non-ambipolar transport and magnetic braking. Calculations indicate a clear δB^2 dependence of NTV, and good agreements with theory on NTV torque profiles and amplitudes depending on collisionality.

This paper is organized as follows; In Sec. II, theoretical formulations and numerical implementation for δf Monte Carlo method are introduced. Benchmarking tests against neoclassical theory and simulations are described in Sec. III. In Sec. IV, non-ambipolar transport in the presence of non-axisymmetric magnetic perturbations are calculated and analyzed applying an analytic magnetic perturbation model. Sec. V describes NTV torque calculation by POCA and comparison results with NTV theory. Summary will be given in Sec. VI.

II. δf MONTE CARLO METHOD FOR NEOCLASSICAL TRANSPORT CALCULATION

This section introduces how δf Monte Carlo method is used in POCA. Theoretical formulations of the Fokker-Planck equation, collision operator, and Hamiltonian equations of motion are described as well as practical implementation. Note that δf Monte Carlo method employed in POCA is based on drift-kinetic equation, thus gyrating particle orbit is a gyro-averaged guiding center motion.

A. Fokker-Planck equation

We start from Fokker-Planck equation,

$$\frac{df}{dt} = \frac{\partial f}{\partial t} + \vec{v} \cdot \frac{\partial f}{\partial \vec{x}} + \frac{\vec{F}}{m} \cdot \frac{\partial f}{\partial \vec{v}} = C(f). \tag{1}$$

The distribution function f can be written as $f = f_M \exp(\hat{f})$ where $\hat{f}$ is a deviation from local Maxwellian f_M. The distribution function can be further approximated to $f \approx f_M(1 + \hat{f})$ since typically $\hat{f} \ll 1$ in fusion plasmas. The Fokker-Planck equation is rewritten using the approximation as

$$\frac{d \ln f_M}{dt} + \frac{d\hat{f}}{dt} = C_m(f). \tag{2}$$

where $C_m(f)$ is a collision operator defined by $C_m(f) = C(f)/f$.

The Fokker-Planck equation is more convenient to solve with δf Monte Carlo method when it is expressed in terms of $\hat{f}$ rather than f. Neglecting external force term $\vec{F}$ in equation (1) and using the local Maxwellian, which is a function of toroidal flux and energy, the Fokker-Planck equation is reduced to

$$\frac{d\hat{f}}{dt} = -\vec{v} \cdot \vec{\nabla}\psi \frac{\partial \ln f_M}{\partial \psi} + C_m(\hat{f}), \tag{3}$$

where ψ is toroidal flux. It is indicated in equation (3) that the deviation from Maxwellian, $\hat{f}$ is proportional to displacement of particles from home flux surface where the test particles are generated. Therefore $\hat{f}$ can be obtained by tracking the guiding center motions of test particles with proper calculation of collision term $C_m(\hat{f})$.

B. Collision operator

A modified pitch angle scattering collision operator, which is composed of Lorentz collision operator and momentum restoring term, is used to calculate the collision term in equation (3) preserving conservation of toroidal momentum. Energy scattering is neglected for computational efficiency and simplicity.

The original Lorentz collision operator representing pitch angle scattering has a following form,

$$C(f) = \frac{\nu}{2} \frac{\partial}{\partial \lambda} \left[\left(1 - \lambda^2\right) \frac{\partial f}{\partial \lambda} \right], \tag{4}$$

where λ is particle pitch defined by $\lambda = v_\parallel / v$ with parallel velocity along the magnetic field line $v_\parallel$, and ν is collision frequency. The Lorentz collision operator in equation (4) conserves energy but does not conserve toroidal momentum. An additional term is required to preserve conserving momentum, which restores the momentum lost by collisions between test particles and background plasmas. One form of the momentum conserving pitch angle collision operator is given by Rosenbluth [7] and Boozer [8] as

$$C_{m.c.}(f) = \nu \frac{m}{B} v_\parallel \frac{\partial}{\partial \mu} \left[\mu \left(v_\parallel \frac{\partial f}{\partial \mu} + \frac{uB}{T} f \right) \right], \tag{5}$$

where B is magnetic field, μ is magnetic moment and T is temperature. The collision operator in equation (5) can be written by using $\mu = m v_\perp^2 / 2B$ and $T = 2/3E$ as

$$C_{m.c.}(f) = \frac{\nu}{2} \frac{\partial}{\partial \lambda} \left[\left(1 - \lambda^2\right) \left(\frac{\partial f}{\partial \lambda} - 3 \frac{u}{v} f \right) \right], \tag{6}$$

where u is mean flow velocity defined by

$$u = \frac{1}{2} \int \hat{f} v_\parallel d\lambda. \tag{7}$$

Practical form of momentum conserving collision operator $C_{m.c.}(f)$ to apply for Monte Carlo method is obtained as a function of $\hat{f}$ by partial derivatives and ignoring subdominant terms [9] as

$$C_{m.c.}(\hat{f}) = \frac{\nu}{2} \frac{\partial}{\partial \lambda} \left[\left(1 - \lambda^2\right) \frac{\partial \hat{f}}{\partial \lambda} \right] + 3\nu \frac{u}{v} \lambda. \tag{8}$$

Now the momentum conserving operator can be implemented by following two steps. First, particle's pitch λ is updated using a Monte Carlo equivalent of the original Lorentz collision operator of equation (4) as

$$\lambda_{new} = \lambda_{old}(1 - \nu\tau) \pm \left[\left(1 - \lambda_{old}^2\right) \nu\tau \right]^{1/2}, \tag{9}$$

where τ is size of time step [10]. The symbol $\pm$ indicates that plus or minus sign is statistically determined by uniformly generated random number. The next step is to bring the momentum restoring term $3\nu\,(v/u)\,\lambda$ of equation (6) into the right hand side of equation (3). Then, $\hat{f}$ is calculated by

$$\Delta\hat{f} = -\Delta\psi \frac{\partial \ln f_m}{\partial \psi} + 3\nu \frac{u}{v} \lambda\tau, \tag{10}$$

which conserves toroidal momentum. The time step τ should be selected to ensure energy conservation during each time step.

C. Hamiltonian equations of motion

The guiding center motion of particles are tracked by Hamiltonian equations of motion. In order to derive orbit equations in non-axisymmetry, it is convenient to use three dimensional spatial coordinates on the flux coordinates and particle pitch. We start from Boozer coordinates [11] by which the magnetic field is expressed as following form,

$$\vec{B} = \frac{\mu_0}{2\pi}\left[G(\psi)\vec{\nabla}\phi + I(\psi)\vec{\nabla}\theta + \beta_*(\psi,\theta,\phi)\vec{\nabla}\psi\right], \quad (11)$$

where μ_0 is the permeability of free space, $G(\psi)$ and $I(\psi)$ are poloidal and toroidal currents, respectively. The drift Lagrangian is written as

$$L = \frac{1}{2}mv_\parallel^2 + \frac{q}{2\pi}\left(\psi\dot{\theta} - \chi\dot{\phi}\right) - \mu B - q\Phi, \quad (12)$$

where q is the electric charge, and Φ is potential. The canonical momenta are

$$p_\theta = \frac{mv_\parallel}{2\pi B}\mu_0 I + \frac{q\psi}{2\pi} = \frac{q}{2\pi}\left(\mu_0 I\rho_\parallel + \psi\right), \quad (13)$$

$$p_\phi = \frac{mv_\parallel}{2\pi B}\mu_0 G - \frac{q\chi}{2\pi} = \frac{q}{2\pi}\left(\mu_0 G\rho_\parallel - \chi\right), \quad (14)$$

where $\rho_\parallel$ is parallel gyroradius defined by $\rho_\parallel = mv_\parallel/qB$. Then, the drift Hamiltonian is written as

$$H = \frac{1}{2}mv_\parallel^2 + \mu B + q\Phi = \frac{q^2B^2}{2m} + \mu B + q\Phi. \quad (15)$$

The orbit equations of motion in terms of $(\theta, \phi, p_\theta, p_\phi)$ are obtained from $\dot{\theta} = \frac{\partial H}{\partial p_\theta}$, $\dot{\phi} = \frac{\partial H}{\partial p_\phi}$, $\dot{p_\theta} = \frac{\partial H}{\partial \theta}$, and $\dot{p_\phi} = \frac{\partial H}{\partial \phi}$ [9].

Hamiltonian equations of motion are more convenient to track the guiding center motions with non-axisymmetry when they are derived in terms of $(\psi, \theta, \phi, \rho_\parallel)$. A set of orbit equations as a function of $(\psi, \theta, \phi, \rho_\parallel)$ are obtained throughout coordinate transforms expressed as following partial derivatives,

$$\dot{\theta} = -\frac{1}{J}\left[\left(\frac{\partial H}{\partial \rho_\parallel}\right)_\psi\left(\frac{\partial p_\phi}{\partial \psi}\right)_{\rho_\parallel} - \left(\frac{\partial p_\phi}{\partial \rho_\parallel}\right)_\psi\left(\frac{\partial H}{\partial \psi}\right)_{\rho_\parallel}\right]_{\theta,\phi}, \quad (16)$$

$$\dot{\phi} = -\frac{1}{J}\left[\left(\frac{\partial H}{\partial \psi}\right)_{\rho_\parallel}\left(\frac{\partial p_\theta}{\partial \rho_\parallel}\right)_\psi - \left(\frac{\partial p_\theta}{\partial \psi}\right)_{\rho_\parallel}\left(\frac{\partial H}{\partial \rho_\parallel}\right)_\psi\right]_{\theta,\phi}, \quad (17)$$

$$\dot{\rho_\parallel} = \frac{1}{J}\left(\frac{\partial p_\phi}{\partial \psi}\right)_{\rho_\parallel,\theta,\phi}\left(\frac{\partial H}{\partial \theta}\right)_{\rho_\parallel,\psi,\phi} - \frac{1}{J}\left(\frac{\partial p_\theta}{\partial \psi}\right)_{\rho_\parallel,\theta,\phi}\left(\frac{\partial H}{\partial \phi}\right)_{\rho_\parallel,\psi,\theta}, \quad (18)$$

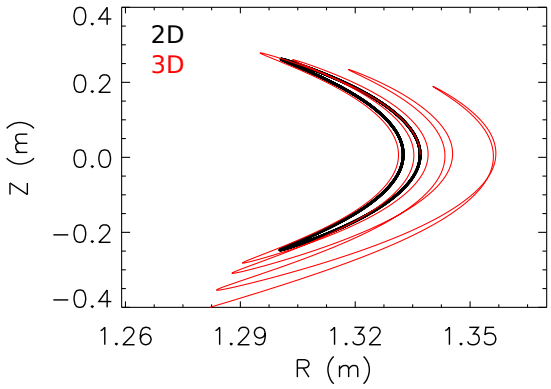

FIG. 1. Trajectories of guiding center orbit of a single particle in axisymmetric and non-axisymmetric configurations. Perfect banana orbit in axisymmetry is distorted by non-axisymmetric perturbations, which cause a shift of banana bounce point.

$$\dot{\psi} = -\frac{1}{J}\left(\frac{\partial p_\phi}{\partial \rho_\parallel}\right)_{\psi,\theta,\phi}\left(\frac{\partial H}{\partial \theta}\right)_{\rho_\parallel,\psi,\phi} + \frac{1}{J}\left(\frac{\partial p_\theta}{\partial \rho_\parallel}\right)_{\psi,\theta,\phi}\left(\frac{\partial H}{\partial \phi}\right)_{\rho_\parallel,\psi,\theta}, \quad (19)$$

where the Jacobian J is defined as $J = (q/2\pi)^2\mu_0(G+\iota I)$ with rotational transform ι. The final form of the Hamiltonian equations of motion are given in the reference [9].

D. Numerical implementation

In order to practically solve the Fokker-Planck equation with δf Monte Carlo method described in the previous section, POCA goes through two steps of orbit and collision step. In the orbit step, a number of test particles ($\geqslant 10^4$) are generated at home flux surface ψ_0 where neoclassical quantities are calculated. Poloidal and toroidal positions are randomly determined by random number generator in order to distribute the test particles uniformly in the poloidal and toroidal spaces. Initial pitches are uniformly distributed in the range of $-1 \leq \lambda \leq 1$ and given to each particle. Test particle's energy distribution is selected to be monoenergetic or Maxwellian. In this study, monoenergetic distribution is used for computational efficiency and simplicity. After the initialization, particles' guiding center motions are solved by Hamiltonian equations of motion. Fourth order Runge-Kutta scheme is applied for time integration of Hamiltonian variables during the orbit step. Next, a collision step followed by orbit step updates particle's pitch and calculate $\hat{f}$ to conserve momentum by equation (10).

POCA is a local code, which means POCA calculates the neoclassical properties locally at the home flux surface. Thus it is required to define an annulus representing the home flux surface. The annulus should be narrow but sufficiently wide to ensure that particles do not leave the annulus in several collision times. Particles leaving

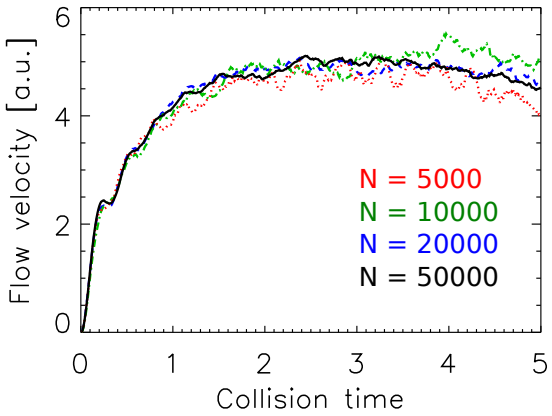

FIG. 2. Time histories of toroidal mean velocity with various number of test particles. The flow velocity reaches an asymptotic value in several collision times with better convergence and less noise as test particle number increases.

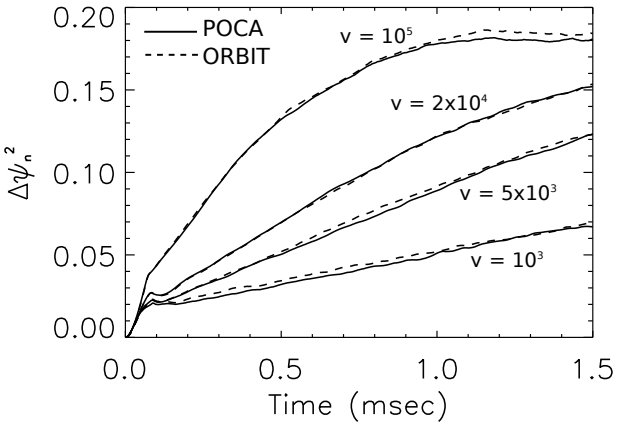

FIG. 3. Time histories of particle displacement $\Delta\psi_n^2$ from POCA (solid) compared with ORBIT (dashed) in the different collision frequencies.

the annulus are reinserted at the home flux surface with re-generated random ψ, θ, ϕ, and λ to maintain the total particle number. After one cycle of orbit and collision step, a new $\hat{f}$ and resultantly δf is obtained by $\delta f = f_M \hat{f}$, which is used to calculate the actual neoclassical transport properties. Even though δf code is much faster than standard Monte Carlo code, the computational cost is still expensive. POCA is parallelized by using MPI packages so that the computation speed is significantly enhanced, and this allows a larger number of test particles and/or simultaneous calculations at multiple flux surfaces.

One of primary results of POCA is a single guiding center orbit motion. POCA reproduces various guiding center orbits such as passing, barely trapped, and trapped particles depending on magnetic field, particle energy and initial pitch. For instance, figure 1 presents trajectories of guiding center orbit of a single particle in axisymmetric and non-axisymmetric configurations. Non-axisymmetric perturbation was applied by equation (30) with $\epsilon = 0.05$ in a typical NSTX plasma. Trapped particle draws a perfect banana orbit in axisymmetry, however a shift of banana bounce point are found in non-axisymmetry as shown in figure 1.

III. BENCHMARKING

Various benchmarking tests for neoclassical transport calculation are described in this section. Axisymmetric configuration is used for comparison of POCA results with neoclassical theory and simulation.

A. Convergence

Convergence of POCA is tested by varying test particle number. Total number of test particles is the only variable while background plasma conditions and initial energy of test particle are fixed in the axisymmetry. Figure 2 shows the time histories of toroidal flow velocity which is an example of neoclassical transport property calculated by POCA. It is clearly observed that the flow velocity reaches an asymptotic value in several collision times regardless of the number of test particles. However the noises significantly decrease as the number of particles increases, which confirms a good convergence of POCA when sufficient test particles are used.

B. Diffusion

Diffusion calculated by POCA is benchmarked with ORBIT code [12], which is well known guiding center code. Figure 3 shows time histories of $\Delta\psi_n^2$, which is a square of displacement of normalized toroidal flux, in the various collision frequencies. Number of the test particle in the range of $5000 \leqslant N \leqslant 20000$ is used to ensure that test particles are confined in the plasma region for sufficient collision times. Therefore $\Delta\psi_n^2$ in figure 3 is an average over N particles. It is observed that particles fill a small area at first, which is approximately the banana orbit width, then diffuse in the radial direction. Good agreements of particles' displacements are found between POCA and ORBIT in the various collision frequencies, which indicates POCA describes the guiding center motion accurately.

For more quantitative comparison, diffusion coefficient of guiding center is defined as

$$D = \frac{d(\Delta\psi_n^2)}{dt}, \tag{20}$$

The diffusion coefficient calculated from both POCA and ORBIT is equivalent to the time derivative of square of particles' displacements, which is a slope of $\Delta\psi_n^2$ after filling the orbit width in figure 3. The calculated diffusion coefficients by POCA also agree very well with ORBIT

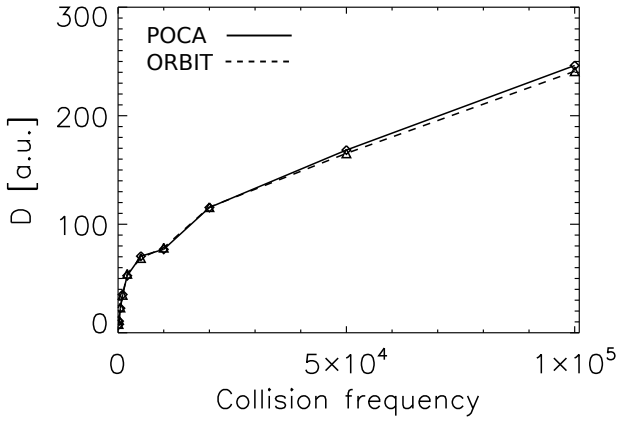

FIG. 4. Calculated diffusion coefficient from POCA (solid) compared to ORBIT code (dashed) as a function of collision frequency. Diffusion coefficients defined as the slope of $\Delta\psi_n^2$ show very good agreements with ORBIT in the wide range of collision frequencies.

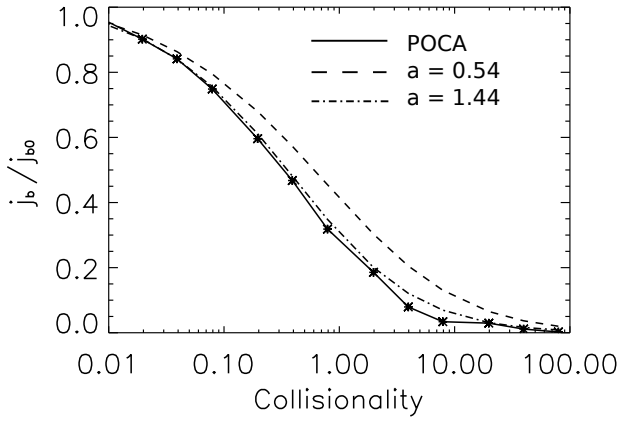

FIG. 5. Normalized bootstrap current scaling as a function of collisionality. Bootstrap current is normalized to the bootstrap current at low collisionality $\sim 10^{-3}$. POCA calculation shows good agreements with theory prediction (dashed) and a scaling from another δf code (dash-dot).

in the wide range of ion-ion collision frequencies as shown in figure 4.

Theoretically predicted Pfirsch-Schlüter, plateau, and banana regimes are observed in figure 4, however the plateau regime is found to be weak compared to other regimes unlike theoretical predictions. Theory predicts the plateau regime exists at $\epsilon^{3/2} \leq \nu_* \leq 1$. Since this benchmarking case uses a high aspect ratio plasma with $\epsilon \sim 0.1$ thus $\epsilon^{3/2} \sim 0.03$ so the plateau regime should be strong. Calculation indicates that it might be difficult to clearly identify the plateau regime by guiding center orbit codes employing only ion-ion collisions.

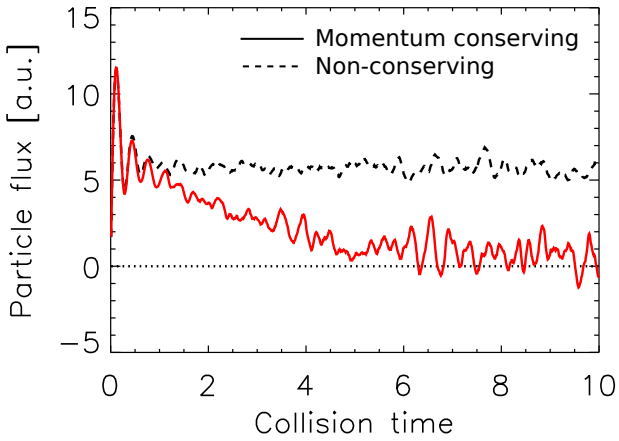

FIG. 6. Time histories of radial particle flux with modified momentum conserving collision operator (solid) and original Lorentz operator (dashed). The particle flux vanishes with momentum conserving collision operator as expected from theory while a finite flux remains with non-conserving operator even in axisymmetry.

C. Bootstrap current

Another benchmarking is performed for bootstrap current. POCA calculates ion bootstrap current automatically. Bootstrap current is defined by

$$j_b = \left\langle \frac{j_\parallel}{B} \right\rangle B_0 \tag{21}$$

where $j_\parallel = qu$. The brackets $\langle\rangle$ denotes the flux surface average. Figure 5 scales the bootstrap current by POCA as a function of collisionality defined by $\nu_* = \nu q R_0/\epsilon^{2/3} v_{th}$ where ϵ is inverse aspect ratio and v_{th} is thermal velocity.

Hinton and Rosenbluth [13] found the dependence of bootstrap current on collisionality as

$$j_b \propto \frac{1}{1 + \sqrt{\nu_*} + a\nu_*}, \tag{22}$$

with $a = 0.54$. Results from another δf code [14] indicates the similar dependence of bootstrap current on collisionality except the coefficient $a = 1.44$. Scaled bootstrap current agrees well with the predictions from theory and modeling as shown in figure 5.

D. Momentum conservation

Conservation of toroidal momentum is critical to separate non-axisymmetric effect from axisymmetric one in transport, since it suppresses particle transport by collisions and drifts in axisymmetric configuration. Therefore the non-ambipolar transport driven by non-axisymmetric perturbations can be distinguished from the transport driven in the axisymmetry by conserving the toroidal

momentum. The easiest way to test whether momentum is conserved by the collision operator is to check the particle flux across the flux surface in the axisymmetry.

The radial particle flux Γ is calculated by

$$\Gamma = \left\langle \int \vec{v_d} \cdot \vec{\nabla}\psi \delta f d^3v \right\rangle, \tag{23}$$

where v_d is drift velocity. The radial particle flux should vanish when it is driven only by like-particle collisions with axisymmetry since an inward particle flux is generated to conserve momentum. Figure 6 shows time histories of particle flux in the axisymmetric configuration with modified momentum conserving operator and non-conserving Lorentz operator. Particle flux with momentum conserving operator vanishes in several collision times while a finite flux remains with non-conserving operator even in the axisymmetry. It is confirmed that the modified pitch angle scattering collision operator used in POCA conserves the toroidal momentum as it should.

IV. NON-AMBIPOLAR TRANSPORT

Axisymmetric magnetic surfaces can be deformed by non-axisymmetric magnetic perturbations. The non-ambipolar transport driven by non-axisymmetric perturbations is important since very small perturbation can change the conventional neoclassical transport significantly. In this section, the non-ambipolar particle transport is measured in the perturbed tokamak and the effects of magnetic perturbations on transport are analyzed.

POCA is developed to easily handle the non-axisymmetric magnetic field information. For instance, POCA can read axisymmetric equilibrium from ESC and EFIT, and non-axisymmetric perturbation information from IPEC and analytic model. The axisymmetric equilibrium field and non-axisymmetric perturbations are combined to give total non-axisymmetric magnetic field as

$$B\left(\psi, \theta\, \phi\right) = B_{2D}\left(\psi, \theta\right)\left[1 + \sum_{mn} \delta_{mn} \cos\left(m\theta - n\phi\right)\right], \tag{24}$$

where δ_{mn} is a strength of perturbation by each (m, n) mode.

In order to separate resonant effect from non-resonant one, an analytic non-axisymmetric perturbation model applying a single resonant mode, expressed as

$$B\left(\psi, \theta\, \phi\right) = B_{2D}\left(\psi, \theta\right)\left[1 + \delta_{mn} \cos\left(m\theta - n\phi\right)\right], \tag{25}$$

was superimposed to axisymmetric equilibrium field provided by ESC where $q_0 = 1.05$ and $q_a = 2.8$. ESC equilibrium solver [15] is used to create the axisymmetric equilibrium $B_{2D}(\psi, \theta)$ using prescribed pressure and safety factor profiles. Analytic non-axisymmetric perturbation model applies a single mode resonating at $q = m/n$ rational surface, thus $m/n = 2/1$ mode resonates at $q = 2$ flux surface. Non-ambipolar particle flux around $q = 2$ flux surface on the model perturbation was calculated with scanning the poloidal mode number from -6 to 10 and fixing toroidal mode number $n = 1$. Various collision frequencies are selected from 20 to 2000, and collisionality is resultantly in the range of $0.012 \leq \nu_* \leq 1.2$. The non-axisymmetric magnetic perturbation strength δ_{mn} is selected as 0.02 and 0.05, which are stronger than conventional experiments but more useful to show clear non-axisymmetric effect on transport.

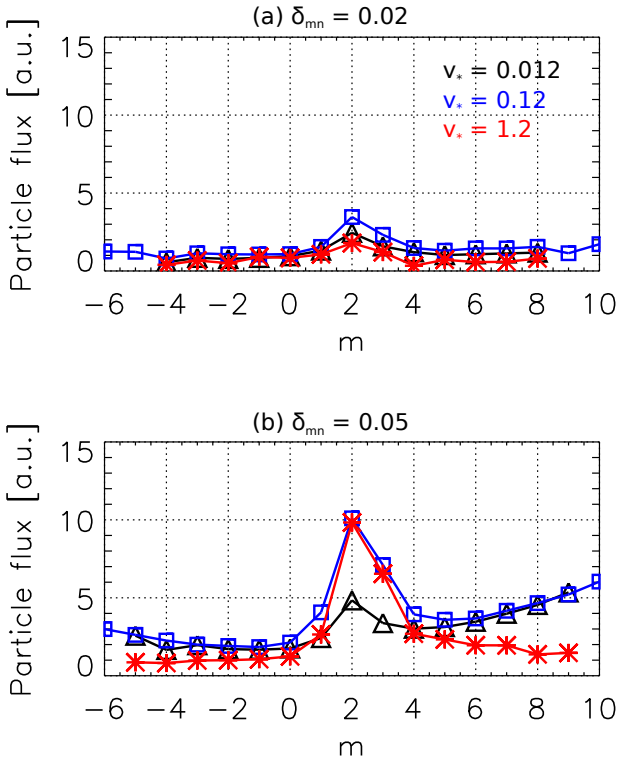

FIG. 7. Non-ambipolar particle flux by $(-6 \leq m \leq 10, n = 1)$ perturbations around $q = 2$ flux surface for (a) $\delta_{mn} = 0.02$ and (b) $\delta_{mn} = 0.05$. The peak particle flux by $(m = 2)$ resonant perturbation clearly indicates the resonant nature of magnetic braking, which is typically considered as non-resonant.

Calculation results indicate that the resonant perturbation significantly enhances the non-ambipolar particle flux as shown in figure 7. The non-resonant perturbations also enhance the particle flux however their effects are generally weaker than the resonant one. It is also clear from figure 7 that stronger perturbation leads to stronger non-ambiploar transport for both resonant and non-resonant modes. The enhanced non-ambipolar particle flux is directly correlated to the magnetic braking driven by NTV since the non-ambipolar flux is proportional to the NTV torque [16]. The non-ambipolar transport, thus NTV transport by non-axisymmetric perturbations provides an additional channel for toroidal mo-

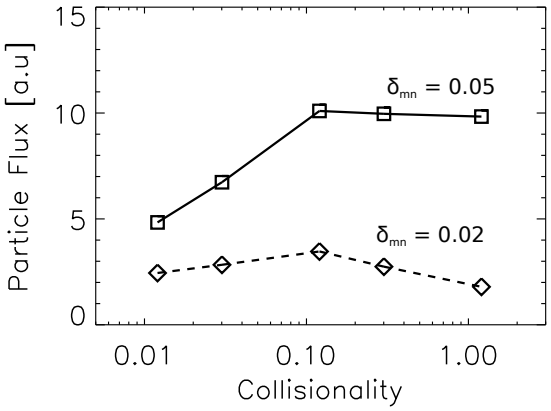

FIG. 8. Peak non-ambipolar particle flux by $m/n = 2/1$ resonant perturbation as a function of collsionality. Peaks are found around $\nu_{ast} \sim 0.1$ similarly with theory.

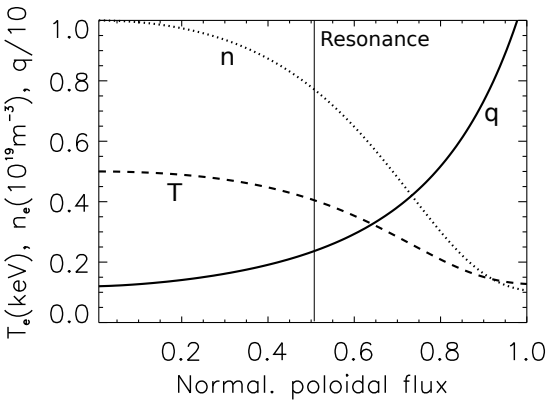

FIG. 9. Kinetic profiles of temperature, density, and safety factor used for benchmarking of NTV torque. Density profile with $n_0 = 1.0 \times 10^{19}$ is drawn in the figure. n_0 is changed for collisionality scan but the profile shape is the same for every collisionality. Vertical line indicates a resonant flux surface at $q = 7/3$.

mentum transport in tokamaks, and the magnetic braking is caused by a modification of toroidal rotation by magnetic perturbations. Therefore the observed significant enhancement of non-ambipolar particle flux by resonant perturbation clearly indicates a strong resonant nature of magnetic breaking, which is typically considered as non-resonant. This trend can be stronger by plasma response to magnetic perturbations, which mostly amplifies resonant modes.

Figure 8 shows dependence of the peak particle flux driven by $m/n = 2/1$ resonant perturbation on collisionality. It is observed that the particle flux increase as collisionality increases, reaches maximum around $\nu_* = 0.1$, and then slowly decreases. Such a trend is consistent with non-ambipolar transport theory and modeling, which might be associated with a bifurcation of the superbanana-plateau and $1/\nu$ regimes.

V. NEOCLASSICAL TOROIDAL VISCOSITY

POCA can directly calculate NTV torque, which is beneficial to clarify the resonant nature of magnetic braking. In general, the NTV torque is expressed by anisotropic pressure tensor as

$$\left\langle \hat{\phi} \cdot \nabla \cdot \overleftrightarrow{P} \right\rangle = \left\langle \frac{1}{2} \frac{\partial \delta P}{\partial \phi} \right\rangle \left\langle \frac{\delta P}{B} \frac{\partial B}{\partial \phi} \right\rangle, \tag{26}$$

where the anisotropic pressure δP is defined by

$$\delta P = \int d^3v \left(\frac{1}{2} m v_\perp^2 + m v_\parallel^2 \right) \delta f. \tag{27}$$

The NTV torque can be calculated with δf Monte Carlo method throughout calculating the anisotropic pressures and utilizing the spectrum of magnetic perturbations [17, 18]. When expressing the non-axisymmetric magnetic perturbations with Fourier series as

$$\frac{\delta B}{B_0} = \sum_{mn} \delta_{mn} (\psi) \cos (m\theta - n\phi), \tag{28}$$

the NTV torque is calculated by following equation [17–19]

$$\left\langle \hat{\phi} \cdot \nabla \cdot \overleftrightarrow{P} \right\rangle = B_0 \sum_{mn} n \delta_{mn} \left\langle \frac{\delta P}{B} \sin (m\theta - n\phi) \right\rangle. \tag{29}$$

Thus the NTV torque in POCA is a sum of toroidal torques driven by each (m, n) Fourier component of magnetic perturbations.

The NTV torque calculation with POCA is compared with a generalized NTV theory derived from a bounce-averaged drift-kinetic equation [5]. Circular plasmas of large aspect ratio is assumed, and $R = 10m$, $a = 2.5m$, and $B_0 = 10T$ are chosen for comparison. A single mode magnetic perturbation expressed by

$$\frac{\delta B}{B_0} = \epsilon \psi_n^2 \cos (7\theta - 3\phi) \tag{30}$$

where ψ_n is normalized poloidal flux and ϵ is fixed as 0.02. The perturbation strength $\delta B/B_0$ is a function of radial coordinates so $\delta B/B_0$ is order of 10^4 at core and 10^2 at edge to be consistent with experiments.

Kinetic profiles of temperature, density, and safety factor used to construct an axisymmetric equilibrium with ESC are drawn in figure 9. Safety factor profile is modeled by $q(\rho) = 1.2 + 9.8\rho^2$ where $\rho = \sqrt{\psi_n}$, therefore $m/n = 7/3$ mode resonates at $q = 7/3$ surface around $\psi_n \sim 0.5$ as indicated by vertical line in figure 9. This benchmarking case is identical to that of FORTEC-3D with the same theory [20] except that deuterium species is considered in this calculation. Density profile is prescribed as $n(\rho) = n_0(n_1 + n_2 \exp(-n_3 \rho^{n_4}))$ with $n_1 = 0.1$, $n_2 = 0.9$, $n_3 = 5.0$, and $n_4 = 4.0$. The density at magnetic axis n_0 is varied from 2.5×10^{17} to 2.5×10^{19} with fixed temperature profile and $T_0 = 0.5keV$, thus collisionality varies in the range of $10^{-2} < \nu_* < 10^1$ depending

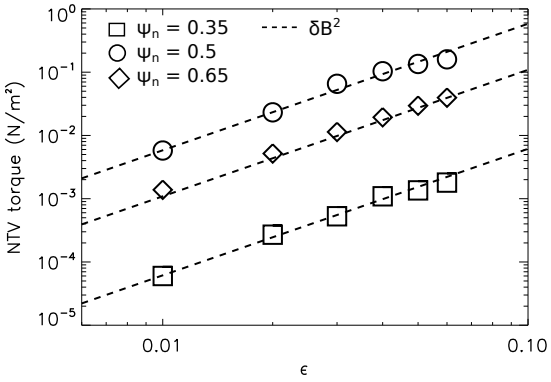

FIG. 10. Dependence of NTV torque on magnetic perturbation strength. The same δB^2 dependence predicted by theory is found by POCA at the resonant and non-resonant flux surfaces.

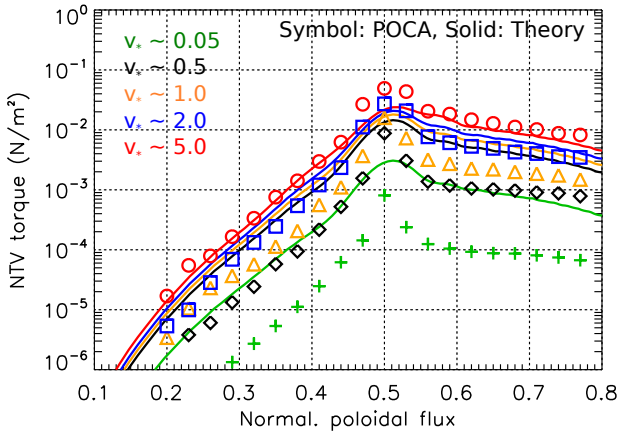

FIG. 11. Benchmark of NTV torque from POCA (symbol) with a theory (solid line). Peak NTV torques are clearly observed around resonant surface at $\psi_p = 0.5$ regardless of collisionality, and they are reduced dramatically at the non-resonant surfaces. The calculated profile shape shows good agreements with theory, but discrepancies exist depending on collisionality, in particular, in the low collisionality regime.

on radial position for each n_0. Note n_0 is changed for collisionality scan but the density profile shape is the same for every collisionality. Electric potential is currently neglected, thus $E \times B$ rotation is assumed to be zero in this study.

One of essential features of NTV transport is found from a scaling of NTV torque against magnetic perturbation strength. The calculated NTV torque is scaled with the perturbation strength ϵ using $n_0 = 1.0 \times 10^{19}$. Figure 10 shows NTV dependence at $\psi_p = 0.5$ where nearby resonant surface and at $\psi_p = 0.35, 0.65$ where non-resonant. The scaling clearly indicates that NTV follows a δB^2 dependence at both resonant and non-resonant flux surfaces, which is consistent with the theory prediction [5, 21].

Comparison results of NTV torque profiles between POCA and the generalized theory show good agreements within an order of magnitude depending on collisionality. NTV torque profiles calculated by POCA with varied n_0 are drawn together with theory prediction in figure 11. Overall trend of NTV profiles at the resonant and non-resonant surfaces are very similar between POCA and theory. Peak NTV torque reasonably agrees with each other in the wide range of collisionality. Biggest discrepancy exists in the low collisionality regimes, however NTV torques around resonant surfaces still show reasonable agreements. Peak NTV torques nearby resonant flux surface indicate the clear resonant nature of the magnetic braking driven by NTV transport.

It should be noted that the magnetic perturbations in theory are applied on Hamada coordinates while the perturbations are on Boozer coordinates in POCA. Therefore the perturbation spectra are slightly different between POCA and theory. The difference in coordinates can be negligible in the core region but it could be larger in the edge region. It is also notable that theory uses Krook collision operator which is largely simplified. Difference in coordinate system of perturbation spectra and collision operator may cause the discrepancies between POCA and theory as similarly as FORTEC-3D differs from theory in reference [20]. In spite of the discrepancy, POCA reflects an essential physics of NTV transport such as δB^2 dependence and the resonant peak consistently with theory, and more realistic physics models embedded in POCA is beneficial for NTV analysis.

VI. SUMMARY

A new δf particle orbit code POCA has been developed to calculate neoclassical transport in the perturbed tokamaks. POCA employes a δf Monte Carlo method with the modified Lorentz collision operator conserving toroidal momentum. Neoclassical transport properties such as diffusion and bootstrap current were successfully benchmarked in the axisymmetric configuration. Non-axisymmetric neoclassical transports such as non-ambipolar particle flux and NTV torque were calculated and compared with theory using an analytic non-axisymmetric perturbation model. POCA reveals clear resonant nature of non-ambipolar transport, NTV, thus magnetic braking. The successful benchmarking results support that POCA can be applicable with its computational benefit for transport analysis in experiment as well as theory study in the presence of non-axisymmetric magnetic perturbations.

ACKNOWLEDGMENTS

The author K. Kim would like to thank Roscoe White for benchmarking with ORBIT code and Stephane Ethier for parallelization of POCA. The private communication with Seung-Hoe Ku was a great help. This work was supported by DOE Contract DE-AC02-09CH11466.

[1] K. Ikeda, Nucl. Fusion **47**, S1 (2007).
[2] A. H. Boozer, Phys. Fluids **23**, 2283 (1980).
[3] K. C. Shaing, Phys. Plasmas **10**, 1443 (2003).
[4] K. C. Shaing, P. Cahyna, M. Becoulet, J.-K. Park, S. A. Sabbagh, and M. S. Chu, Phys. Plasmas **15**, 082506 (2008).
[5] J.-K. Park, A. H. Boozer, and J. E. Menard, Phys. Rev. Lett. **102**, 065002 (2009).
[6] J.-K. Park, A. H. Boozer, and A. H. Glasser, Phys. Plasmas **14**, 052110 (2007).
[7] M. N. Rosenbluth, R. D. Hazeltine, and F. L. Hinton, Phys. Fluids **15**, 116 (1972).
[8] A. H. Boozer and H. J. Gardner, Phys. Fluids B **2**, 2408 (1990).
[9] M. Sasinowski and A. H. Boozer, Phys. Plasmas **4**, 3509 (1997).
[10] A. H. Boozer and G. Kuo-Petravic, Phys. Fluids **24**, 851 (1981).
[11] A. H. Boozer, Phys. Fluids **24**, 1999 (1981).
[12] R. B. White and M. S. Chance, Phys. Fluids **27**, 2455 (1984).
[13] F. L. Hinton and M. N. Rosenbluth, Phys. Fluids **14**, 836 (1973).
[14] M. Sasinowski and A. H. Boozer, Phys. Plasmas **2**, 610 (1995).
[15] L. E. Zakharov and A. Pletzer, Phys. Plasmas **6**, 4693 (1999).
[16] K. C. Shaing, Phys. Fluids **26**, 3315 (1983).
[17] J. L. V. Lewandowski, J. Williams, A. H. Boozer, and Z. Lin, Phys. Plasmas **8**, 2849 (2001).
[18] J. D. Williams and A. H. Boozer, Phys. Plasmas **10**, 103 (2003).
[19] S. Satake, H. Sugama, R. Kanno, and J.-K. Park, Plasma Phys. Control. Fusion **53**, 054018 (2011).
[20] S. Satake, J.-K. Park, H. Sugama, and R. Kanno, Phys. Rev. Lett. **107**, 055001 (2011).
[21] J.-K. Park, Phys. Plasmas **18**, 110702 (2011).

The Princeton Plasma Physics Laboratory is operated
by Princeton University under contract
with the U.S. Department of Energy.

Information Services
Princeton Plasma Physics Laboratory
P.O. Box 451
Princeton, NJ 08543

Phone: 609-243-2245
Fax: 609-243-2751
e-mail: pppl_info@pppl.gov
Internet Address: http://www.pppl.gov